FUTURES ISSUE: INORGANIC MATERIALS: SYNTHESIS AND PROCESSING

Check for updates



Enhancing magnetic hyperthermia in ferrite nanoparticles through shape anisotropy and surface hybridization

| Rohini Thevi Guntnur¹ | Jason Guiliani² | Gabriela Romero¹ o Gloria L. Jiménez¹

²Department of Physics and Astronomy, University of Texas at San Antonio. One UTSA Circle, San Antonio, Texas, USA

Correspondence

Gabriela Romero, Department of Biomedical Engineering and Chemical Engineering, University of Texas at San Antonio. One UTSA Circle, San Antonio, TX 78249, USA. Email: gabrielaromero.uribe@utsa.edu

Funding information

National Science Foundation, Grant/Award Number: CBET - 2044713; The University of Texas System and Mexico's Conseio Nacional de Ciencia y Tecnología through the ConTex Postdoctoral Fellowships Program

Abstract

Magnetic hyperthermia has been studied for the past two decades in cancer treatments as the local heat generated by magnetic nanoparticles under applied alternating magnetic fields is sufficient to kill cancer cells. More recently, it has been explored for controlling biological signaling through heat-sensitive transmembrane channels. It is of great interest to produce magnetic nanoparticles with high heat transducing efficiency to minimize potential off-target heating effects. Here, we describe shape anisotropy and particle hybridization as possible routes to augment magnetic hyperthermia in ferrite nanoparticles. Zinc substituted magnetite core and core-shell cubic nanoparticles with different sizes were synthetized. It was found that nanoparticles shape and composition are altered from cubic to flower-like, and to a more franklinite rich phase as size increased. Hybridization with a cobalt shell allowed to enhance nanoparticle magnetic coercivity and specific power loss. The optimized core-shell nanoparticles were tested to induce cellular activity in hippocampal neurons.

TOPICAL HEADING: Inorganic Materials: Synthesis and Processing.

KEYWORDS

coercivity, hybridization, magnetic hyperthermia, magnetic nanoparticles, shape anisotropy

INTRODUCTION 1

Magnetic nanoparticles (MNPs) are one of the most promising materials in nanotechnology due to their unique physical properties that lead to a wide variety of applications ranging from data storage^{1,2} to MRI contrast enhancement agents,³⁻⁵ nanosensors,⁶⁻⁸ and drug delivery carriers^{9,10} among others. MNPs size, shape, and composition can be tailored through well-established, economic, and sustainable synthetic protocols. 11-15 Frequently MNPs are composed of iron oxides because of their superparamagnetic behavior, low toxicity, inexpensive price, and synthesis versatility. 16,17 Iron oxide exists in three different magnetic phases: fully oxidized-maghemite (γ -Fe₂O₃), mixed valance Fe^{2+,3+} magnetite, and reduced metastable wüsite (Fe_xO). All magnetic iron oxide nanoparticles have a facecentered cubic oxygen sublattice but with different coordination state. 3,18,19 The magnetic properties of MNPs composed of iron oxides can be tailored during synthesis by controlling reaction

parameters such as temperature, time, and the nature and ratio of the surfactant, solvent, or precursors. 11,13,20 Control over MNPs' synthesis diminishes the probability of forming undesirable nonmagnetic iron oxide phases. 21,22

Moreover, magnetic materials can be classified as diamagnetic, paramagnetic, or ferromagnetic. Ferromagnetic materials are subclassified as soft and hard ferromagnetic depending on their magnetic coercivity. MNPs with a coercivity <100 Oe are classified as soft ferromagnetic nanomaterials, while MNPs with coercivity >125 Oe are classified as hard nanomaterials. 23,24 One of the most interesting properties of ferromagnetic materials is their ability to transduce alternating magnetic fields (AMF) into heat. This physical phenomenon is known as magnetic hyperthermia (MH), and it is associated with the re-orientation of the nanomaterial's magnetic moment under an applied AMF. The magnetic moment is re-oriented following mechanisms of Brownian rotation, Néel rotation, hysteretic loss, or the combination between them.²⁵⁻²⁸

¹Department of Biomedical Engineering and Chemical Engineering, University of Texas at San Antonio. One UTSA Circle, San Antonio, Texas, USA

MH is one of the most exploited properties of MNPs in the biomedical field. The local heat generated by MNPs has been investigated in cancer therapies to damage and kill cancer cells due to the local high temperatures generated, 5,29,30 and in neural engineering for the remote control of biological signaling. 31,32 In these therapies, high-efficient heat nanotransducers are desired to minimize the potential of off-target heating effects. Although MH and MNPs have been extensively studied in the past decades, obtaining high-efficient materials for heat conversion is the golden standard in colloidal chemistry. Considering magnetic dipoles at the mesoscale it is possible to infer that MNPs' internal structure directly impacts their magnetic heating properties, being defect-free single-crystalline MNPs the "ideal." Due to their large surface to volume ratio, MNPs are very susceptible to structural and compositional defects, making this "ideal" highly challenging. 33 Recently it has been demonstrated that nano and atomistic engineering of MNPs' defects and spin disorders can also maximize MH properties.³⁴ Approaches to systematically engineer defects in single-domain MNPs include the introduction of grain boundaries, the assembly of MNPs' organic frameworks or inducing defects through doping. Hybrid iron oxide MNPs with different morphologies and sizes have been investigated for high energy conversion as doping with other metals can modify the atomic arrangement of the ferrite crystalline structure leading to drastic changes in the magnetic properties of the nanoparticles such as increasing in the coercive field, saturation magnetization, and improving the efficiency to dissipate heat. 11,12,20,29,30,35

Here, we investigate the enhancement of MH by shape and exchange anisotropy in cubic magnetic nanoparticles (CNPs) for core (cCNPs) and core-shell (csCNPs) nanostructures. Our synthesized 29-nm csCNPs composed of a 28-nm ZnFe $_2$ O $_4$ core and a \sim 0.5-nm thick CoFe $_2$ O $_4$ shell displayed a specific loss power of 1139 W/g, one of the highest reported for synthetic ferrite MNPs. These particles were investigated as nanotransducers of AMF to enhance heat-sensitive ion channels located in the cell membrane of primary hippocampal neurons. The heat dissipated by csCNPs allowed to evoke neural activity in hippocampal cultures utilizing up to $100\times$ less quantity of particles than what it was used in previously reported investigations that utilize ferrite single domain spherical nanoparticles. 31,36 Finally, it was observed that these csCNPs and the applied AMF cause no cytotoxic effects.

2 | EXPERIMENTAL

2.1 | Materials

Iron (III) acetylacetonate (Fe(acac) $_3$ - 97%), and dibenzyl ether (DBE - 98%), sodium chloride (NaCl), deoxyribonuclease I (DNAse I), and papainase were purchased from Sigma-Aldrich. Zinc (II) acetylacetonate (Zn(acac) $_2$ 95%), cobalt (II) acetylacetonate (Co(acac) $_2$ - 99%), poly (acrylic acid) (PAA - 63%) with a molecular weight of 2000 Dalton, ethyl alcohol (99.5), hexane (95%), and acetone (99.6) were supplied by Acros Organics. Oleic acid (OA - 90%), potassium chloride (KCl) and magnesium

sulfate (MgSO₄) were obtained from Alfa Aesar. Diethylene glycol (DEG), HPLC grade water, and 4-(2-hydroxyethyl)-1-piperazineethanesulfonic acid (HEPES) were purchased from Fisher Scientific. Calcium chloride (CaCl₂) and sodium hydroxide (NaOH) were purchased from Merk. Neurobasal A medium, B-27 supplement, glutamax-I supplement, and trypan blue were acquired from Gibco. Fetal bovine serum, and MITO+ serum extender were bought from Corning. Fluo-4 Direct™ Calcium Assay Kit was purchased from Thermo Fisher Scientific. Glucose was obtained from Macron fine chemicals, L-Cysteine from MP Biomedicals, EDTA from IBI Scientific, and trypsin inhibitor from Roche.

2.2 Nanoparticles' synthesis and functionalization

cCNPs were synthesized using a protocol adapted from Noh et al. ¹² Briefly, Fe(acac)₃ and Zn(acac)₂ at different molar concentrations were place in a 50 ml three-neck round-bottom flask in the presence of OA (4 mmol) and DBE (53 mmol). The mixture was refluxed at 290°C for 30 min under N₂ gas. The metal precursors molar concentrations tested were 0.7, 0.8, 0.9, and 2.0 mmol of Fe(acac)₃ with 1.05, 1.2, 1.35, and 3 mmol of Zn(acac)₂, respectively. Particles with sizes varying from 28 to 100 nm were obtained. These particles are identified in this paper by their size in nanometers, that is, XX nm cCNPs.

csCNPs were synthesized using seed grown technique. Briefly, 30 mg of cCNPs (28 or 35 nm) were dispersed in 4 ml of hexane and sonicated for 30 min. Separately, a mixture of 0.36 mmol Fe(acac)₃ and Co(acac)₂ at different concentrations (0.1, 0.53, 1.42, and 0.36 mmol) was prepared in 1.1 ml of OA and 17.5 ml of DBE. cCNPs were injected into the mixture and the reaction was heated to 290°C under inert atmosphere and refluxed for 30 min. These particles are identified in this paper by their overall size in nanometers as well as the size of their core-only, being 1 a core of 28 nm and 2 a core of 35 nm, that is, XX nm csCNPs—1 or XX nm csCNPs—2.

Both, cCNPs and csCNPs, were transferred into aqueous solution using a protocol adapted from Zhang et al. Per each 30 mg of nanoparticles, 30 ml of DEG and 6 ml of PAA were used. First, DEG and PAA were mixed under magnetic stirring and inert atmosphere at 150° C for 30 min. Then core or core-shell nanoparticles dispersed in toluene were injected in the DEG/PAA solution. The mixture was refluxed at 240° C for 3 h under N_2 gas.

A volume of 6 ml of PAA was used as it was found the optimal to maintain colloidal stability. Colloidal stability was evaluated also for nanoparticles stabilized with 2, 4, 6, 8, and 10 ml of PAA at fixed DEG volume.

2.3 | Nanoparticles' morphology

Transmission electron microscopy (TEM) and scanning transmission electron microscopy (STEM) techniques were used to evaluate the morphology and size of cCNPS and csCNPs. A JEOL 1230 TEM and a

Hitachi STEM-5500 instruments were used at 80 and 30 kV, respectively. The specimens were dispersed in hexane and mounted on carbon-coated TEM grids.

2.4 | Nanoparticles' composition

The chemical composition of CNPs was determined by inductively coupled plasma-optical emission spectrometry (ICP-OES) using a PerkinElmer Optima 2100 spectrometer. Chemical composition of CNPs was also characterized by elemental dispersive spectroscopy (EDS) using a Bruker edax unit at a frequency of 40 Hz, and a temperature of 300°K.

Powder x-ray diffraction (XRD) patterns of cCNPS and csCNPs were collected using a Malvern Panalytical difractometer equipped with PIXcele3 detector using CuK α radiation ($\lambda=1.5418$ Å). Phase identification and crystalline parameters were obtained by Rietveld refinement using Topas academic V 3.0 and LaB $_6$ as internal reference (Figure S3).

2.5 | Nanoparticles' magnetic properties

Hysteresis curves were obtained using a Vibrating Sample Magnetometer (VSM) from VersaLab Quantum Design. The samples were measured using a powder container and at room temperature with a frequency of 40 Hz.

Magnetic heating efficiency of cCNPs and csCNPs was evaluated by means of specific loss power (SLP). SLP was measured using a MH system (MSI Automation) with a 5 cm cooper coil to deliver an AMF of 27.3 mT with a frequency of 250 KHz. A microcentrifuge tube containing the tested sample (magnetic fluid at concentration of 1 mg/ml) was placed into the coil and the AMF was applied for 60 s. A Qualitrol Neoptix temperature probe was used to monitor the temperature changes. All the samples were measured three times. SLP was calculated using Equation 1:

$$SLP = \frac{C\rho_s m_s}{m_{NPs}} \left[\frac{\Delta T}{\Delta t} \right], \tag{1} \label{eq:1}$$

where Cp_s is the specific heat capacitance of the suspension, m_s is the mass of the solvent, m_{NPs} is the total mass of magnetic materials (Fe, Zn, and Co), and $\Delta T/\Delta t$ is the initial slope of the heating curve.

2.6 | Primary rat hippocampal culture

Hippocampal neurons were extracted from new-born Sprague Dawley rat brains following Beaudoin et al. protocol. After isolation, hippocampal neurons were dissociated, and plated on 35-mm collagencoated glass bottom tissue culture dishes. Neurons were cultured in neurobasal media supplemented with B-27 at 37° C and 5% CO₂.

Stimulation and control experiments were performed on healthy cultures 10–15 days post isolation.

Prior stimulation hippocampal cultures were stained with Fluo-4 following manufacturer protocols. Then, csCNPs solutions in Tyrode were added to the cultures and exposed to AMF for 60 s. Neural activity was recorded using a fluorescence stereomicroscope (Leica M205 FCA) equipped with $2\times$ and $5\times$ Plan Apo objectives, and a sCMOS camera (Leica DFC9000). The microscope was coupled to the MH system to monitor neural activity in real-time through calcium imaging recording.

2.7 | Analysis of videos

Analysis of the videos recorded was performed using Image J to subtract background and extract the intensity profile of each neuron recorded. A MATLAB code was used to threshold neural activity and extract the activity of 100 random neurons in each group.⁹ Five videos (> 500 neurons) were analyzed per condition tested.

2.8 | Cytotoxicity

Cell viability was determined by standard colorimetric MTT (3-(4,5-dimethylthiazol–2-yl)-2,5-diphenyltetrazolium bromide) assay. 29 nm csCNPs – 1 were suspended in PBS at different concentrations (0–1 mg/ml). csCNPs were added to HEK-293 cells cultured in a 96-well plate (25,000 cells per well). Cell viability was measured at 24, 48 and 72 h of co-culturing. Cell viability was also tested for cells co-cultured with csCNPs and exposed to AMF. Viability was measured 24, 48, and 72 h post AMF stimulation. Briefly, 20 μ l of MTT (5 mg/ml in PBS) were added to each well and allowed to react for 3 h. After, the solution was aspirated and 200 μ l of dimethyl sulfoxide were added. The plate was centrifugated at 5000 rpm per 5 min to eliminate possible interference of the nanoparticles in the absorbance reading. A plate reader was used to measure absorbance at 570 nm.

3 | RESULTS AND DISCUSSION

3.1 | Size and composition of cCNPs and csCNPs

cCNPs were synthetized thorough a coprecipitation method using acetylacetonates of Fe³⁺ and Zn²⁺ as organic precursors, oleic acid as surfactant and dibenzyl ether as dispersant. The reaction was carried out at 290°C for 30 min. Particle size was controlled by varying the molar concentration of each precursor and preserving the same reaction conditions. TEM and STEM were used to characterize the morphology, size, and composition of CNPs. TEM and STEM micrographs of cCNP are shown in Figures 1 and S1, respectively. It was found that by increasing the size of cCNPs from 28 to 100 nm, the cubic morphology is altered toward flower-like nanoparticles. This observation

FIGURE 1 Representative TEM micrographs of cCNPs with different size (cube length): (A) 28 ± 4.5 nm, (B) 35 ± 5.7 nm, (C) 50 ± 5.7 nm, and (D) 100 ± 14 nm. Size was measure through TEM image analysis. Statistically significant differences among the particle size distributions of the groups were found (p < 0.05, one-way ANOVA)

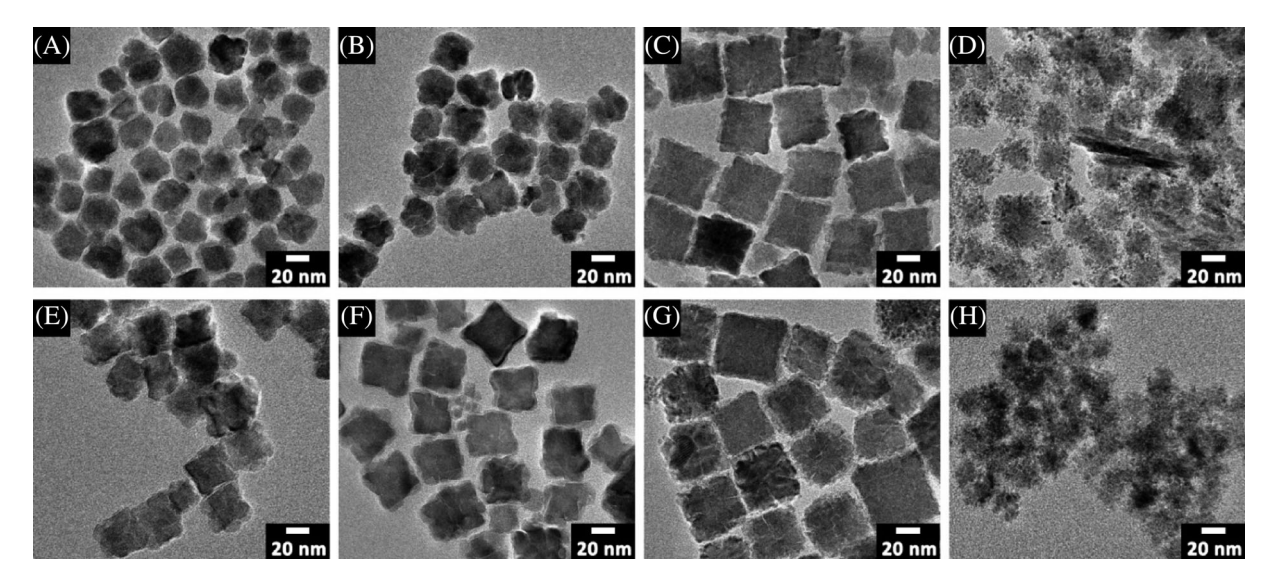


FIGURE 2 Representative TEM micrographs of csCNPs. (A) 29 nm csCNPs - 1, (B) 33 nm csCNPs - 1, (C) 49 nm csCNPs - 1, (D) 29 nm csCNPs - 1, (E) 35 nm csCNPs - 2, (F) 36 nm csCNPs - 2, (G) 46 nm csCNPs - 2, and (H) 28 nm csCNPs - 2

could be a result of an increase in Zn concentration as particle size increases, leading to modifications in the nanoparticle crystalline structure.

csCNPs were synthetized using a seed mediated growth method, where 28 and 35 nm cCNPs were used as a seed to grow a cobalt ferrite (CoFe₂O₄) shell. The shell was grown using acetylacetonate of Fe³⁺ and Co²⁺ as precursors. The shell was synthesized using different Co(acac)₂ concentrations. Regardless the size of the core used, a cubic morphology was observed for csCNPs when the Co concentration in the shell was approximately 26% (Figure 2A, G and S2). When the Co concentration in the shell was lower than 26%, csCNPs exhibited a cubic morphology but with an appreciable surface roughness (Figure 2A, B, E, F and S2). This could potentially result in increased heat transduction efficiency due to the apparent spin disorder.³³ High concentrations of Co in the shell lead to distorted particle morphologies (Figure 2D, H). The change in morphology at higher Co concentrations in the shell could be the result of distinct favored phases such as cobalt iron (CoFe) or siderite. As expected, the Co concentration in the shell was associated with the

thickness of the shell, which varied between 0.8 and 20.4 nm as shown in Figure 2 and Table S2.

EDS and ICP-OES were used to study the elemental composition of CNPs. A summary of the composition of cCNPs measured by both techniques is presented in Figure 3A and in Table S1. Both measurements are consistent within each other having a small deviation of around 4% (not statistically significant, p > 0.05, one-way analysis of variance [ANOVA]). It was observed that the Fe concentration decreased, and the Zn concentration increased as the size of the nanoparticles increased. This results suggest that Zn could be substituting Fe atoms in the magnetite structure, leading to a possible enhancement in the magnetic properties. ^{13,14} EDS analysis for csCNPs (Table S2) showed a similar behavior, the particle size increased as the Co concentration in the shell increased. The increment of Zn and Co concentration in cCNP and csCNPs, respectively, could result in an enhancement of magnetic properties as changes in the nanoparticles' crystallinity will modify the cation distribution of the nanostructures. ^{13–15,20,39}

The crystalline structure of CNPs was investigated by XRD. All compositions found in CNPs were indexed in terms of the single-

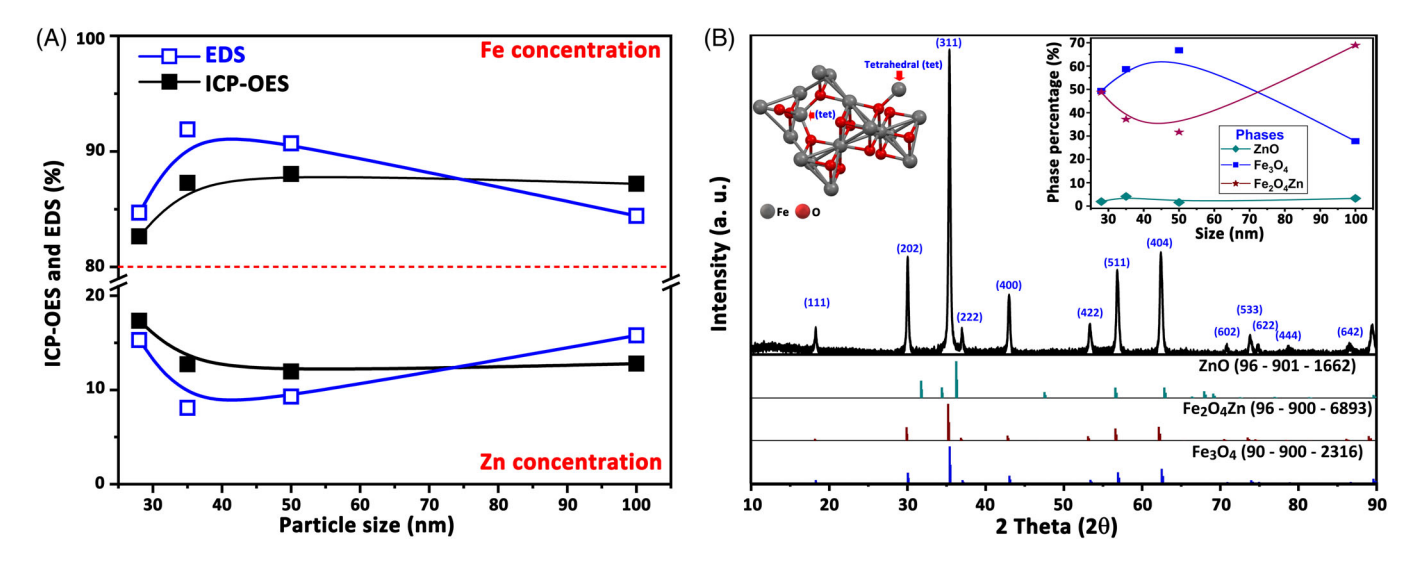


FIGURE 3 Elemental composition of cCNPs as function of their size: (A) measured by ICP-OES and EDS, and (B) XRD pattern of 28 nm cCNPs with Miller indices (hkl) values of magnetite based on 96-900-2316 card. The inset summarizes the phase quantification as a function of nanoparticle size

TABLE 1 Summary of the cCNPs crystallite size parameters obtained from XRD measurements. Lattice constant (A), average crystallite size and ionic radio (r) of tetrahedral (A) and octahedral (B) sites of cCNPs.

cCNPs (nm)	a (Å) of Fe₃O₄	Crystallite size (nm)	r _A (Å)	r _B (Å)
28	8.4073(40)	28.4	0.4702	0.7518
35	8.4145 (40)	36.6	0.4718	0.7536
50	8.4086 (33)	55.3	0.4705	0.7522
100	8.4247 (72)	32.1	0.4740	0.7562

phase cubic spinel structure of magnetite (JCPDS 90-900-2316).40 Figure 3B shows the XRD pattern of 28 nm cCNPs. The strongest peak (311) denotes the spinel phase, while the other peaks, (202), (400), (511), and (404), corroborate the inverse cubic spinel ferrite structure. 39,40 Moreover, XRD refinement shows that cCNPs are composed not only magnetite (Fe₃O₄), but franklinite (ZnFe₂O₄) and zincite (ZnO) phases are also present. The presence of Zn²⁺ ions during synthesis causes that some Fe^{3+} ions in tetrahedral side of the crystal shift toward octahedral sites as Zn²⁺ has stronger preference. This susceptibility changes the cation distribution in the crystallite and could lead to an increase in the magnetic moment of the nanoparticles. 15,19,39-43 cCNPs composition characterized by XRD is summarized in the inset of Figure 3B and Table S3 as a function of nanoparticle size. For cCNPs, Fe₃O₄ is the dominant phase up to a saturation point achieved at the 50 nm size. Then, the formation of franklinite (ZnFe₂O₄) is favored. Diffractograms and structure refinements are shown in Figure S4 and Table S3, where it is possible to observe that the intensity of the main spinel phase attributed to magnetite varies as function of cCNPs size and ZnFe₂O₄ composition. This behavior corroborates the changes in cCNPs crystallinity associated with crystallographic defects induced by Zn substitution as nanoparticle's size increases. 13,14,19

Table 1 summarizes the crystallite size obtained by Rietveld refinement and Match program. The lattice parameters and ionic ratios of oxygen with tetrahedral (A) and octahedral (B) sites of Fe change with cCNPs size due to the different degree of Zn^{2+} substitution. The estimated crystallite sizes from 28 to 50 nm cCNPs are in agreement with the sizes measured by TEM. However, for 100 nm cCNPs there is a significant difference (p < 0.05, Tukey's test) between the size calculated by XDR and the size measured by TEM. This discrepancy can be attributed to the fact that cubic shape is no longer predominant, instead the formation of particles with distorted morphology is favored (Figure 1D,H). Excess of Zn^{2+} ions favor ZnO phase changing the crystallinity of the nanoparticle as it can be observed in Figure S4, where the intensity of the main peak ascribed to magnetite decreases drastically as cCNPs size increases. 39,44

XRD diffraction pattern of 29 nm csCNPs – 1, and the phase composition of csCNPs with different thickness of CoFe $_2$ O $_4$ in the shell obtained using Rietveld refinement are shown in Figure 4. XDR refinement (Figure S5) corroborates the hybridization of csCNPs. The phases identified in csCNPs are Fe $_3$ O $_4$, ZnFe $_2$ O $_4$, ZnO, CoFe $_2$ O $_4$ (JCPDS 95-153-5820), cobalt-zinc ferrite (CoZnFeO) (JCPDS 04-017-8598), CoFe (JCPDS 95-152-4320), and FeCO $_3$ (96-901-4729). The hybridization of csCNPs is confirmed by the presence of ZnFeCoO, CoFe, and

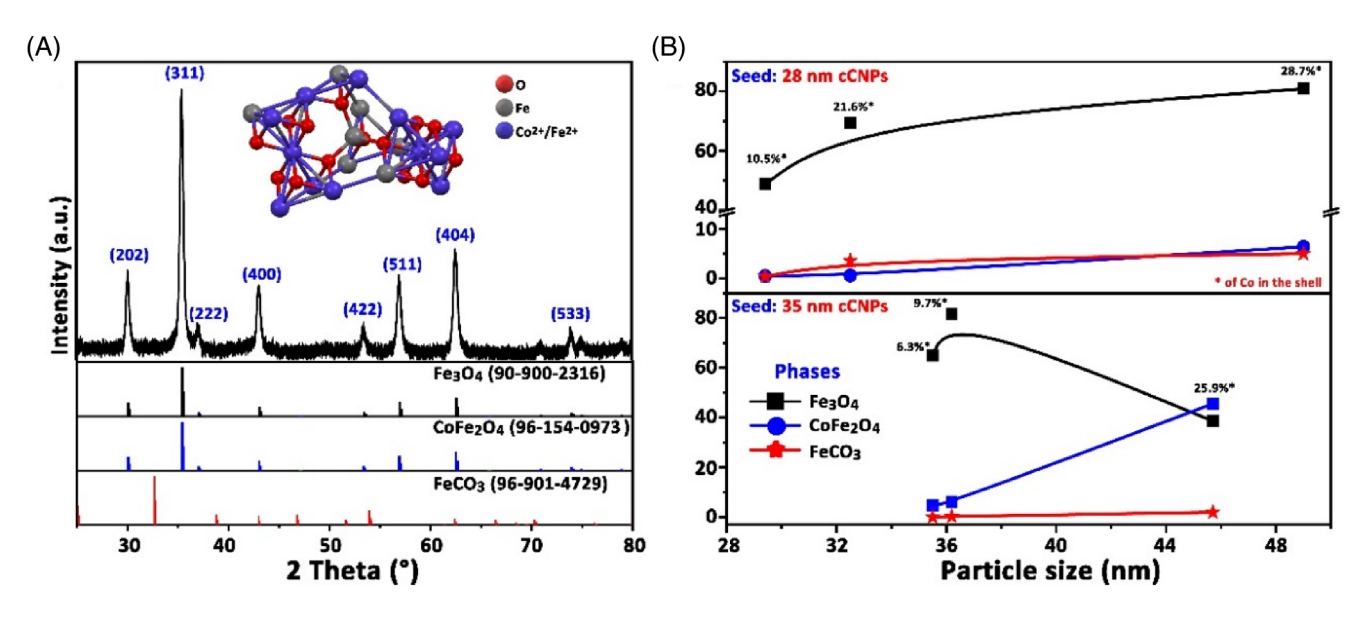


FIGURE 4 Elemental composition of csCNPs. (A) XRD pattern of 29 nm csCNPs – 1, and (B) phase quantification of csCNPs as function of particle size

TABLE 2 Summary of the csCNPs crystallite size parameters obtained from XRD measurements after Rietveld refinement. Lattice constant (a) and volume (V).

Lattice para		arameters	
Sample	<i>a</i> (Å) Fe₃O₄	V (Å ³) Fe ₃ O ₄	Crystallite size (nm) ^a
29 nm csCNPs - 1	8.39	590.94	32.3
33 nm csCNPs - 1	8.40	593.05	35.4
49 nm csCNPs - 1	8.41	594.20	52.4
29 nm csCNPs - 1*	10.30	1090.72	28.3
36 nm csCNPs - 2	8.39	589.70	22.7
36 nm csCNPs - 2	8.40	594.13	46.6
46 nm csCNPs - 2	8.41	593.82	39.6
22 nm csCNPs - 2*	8.41	594.40	20.8

Abbreviation: csCNPs, core-shell cubic magnetic nanoparticles.
^aCalculated using Match software.

FeCO $_3$ phases, and by the increase of the lattice constant as Co concentration increases. The latter caused by the substitution of Fe $^{2+}$ ions in the crystalline structure. Figure S5 shows that at higher Co concentrations (>45%), the csCNP's crystallinity diminishes, and new peaks appear at 31.8° and 36°, ascribed to FeCO $_3$.

Lattice parameters for csCNPs are summarized in Table 2. It is possible to corroborate the same core composition as for cCNPs. Magnetite and franklinite have similar lattice parameters confirming that octahedral sites are partially occupied by Zn^{2+} . The presence of CoZnFeO confirms a successful hybridization process, where the core is composed by Fe and Zn and the shell by Fe and Co compounds. The lattice parameters of CoZnFeO are consistent with that reported

by Varshney et al. (8.3522 Å).⁴² Crystallite sizes of csCNPs calculated from XRD are in agreement with TEM measurements (Table S2).

3.2 | Magnetic properties of cCNPs and csCNPs

The magnetic properties of CNPs were characterized using VSM. Figure 5A shows the hysteresis loops of different size cCNPs. All cCNPs displayed a characteristic profile of ferromagnetic nanomaterials. Saturation magnetization (M_s) and magnetic coercivity (H_c) varied depending on the cCNPs size. Figure 5B summarizes the magnetic properties of the different sized cCNPs. It is possible to observe that M_s increases from approximately 60 to 95 emu/g and H_c from approximately 5 Oe to 40 Oe as the particle size increases up to maximum values reached in 50 nm cCNPs. The enhancement in the magnetic properties as a function of nanoparticle size can be explained by the spin modification ascribed by the substitution of Zn² $^+$ in the magnetite structure. However, M_s and H_c diminish drastically for particles larger than 50 nm as expected for larger grains with more magnetic multidomains. Zn doping in cCNPs was corroborated by the XRD refinement (Figure 3), where it was observed that magnetite formation is favored for up to 50 nm cCNPs, and for larger nanoparticles franklinite phase dominated. For cCNPs above 50 nm the excess of Zn²⁺ in the crystalline structure promotes antiparallel arrangement and the growth of an antiferromagnetic phase (zincite), which triggers a decay in the M_s and H_c values. 45,46 These magnetic properties behavior is coupled with the formation of flower-like nanoparticles

To further modify the surface and exchange anisotropy, cCNPs were coated with a $CoFe_2O_4$ shell to form csCNPs. VSM measurements of csCNPs corroborated that magnetic properties can be

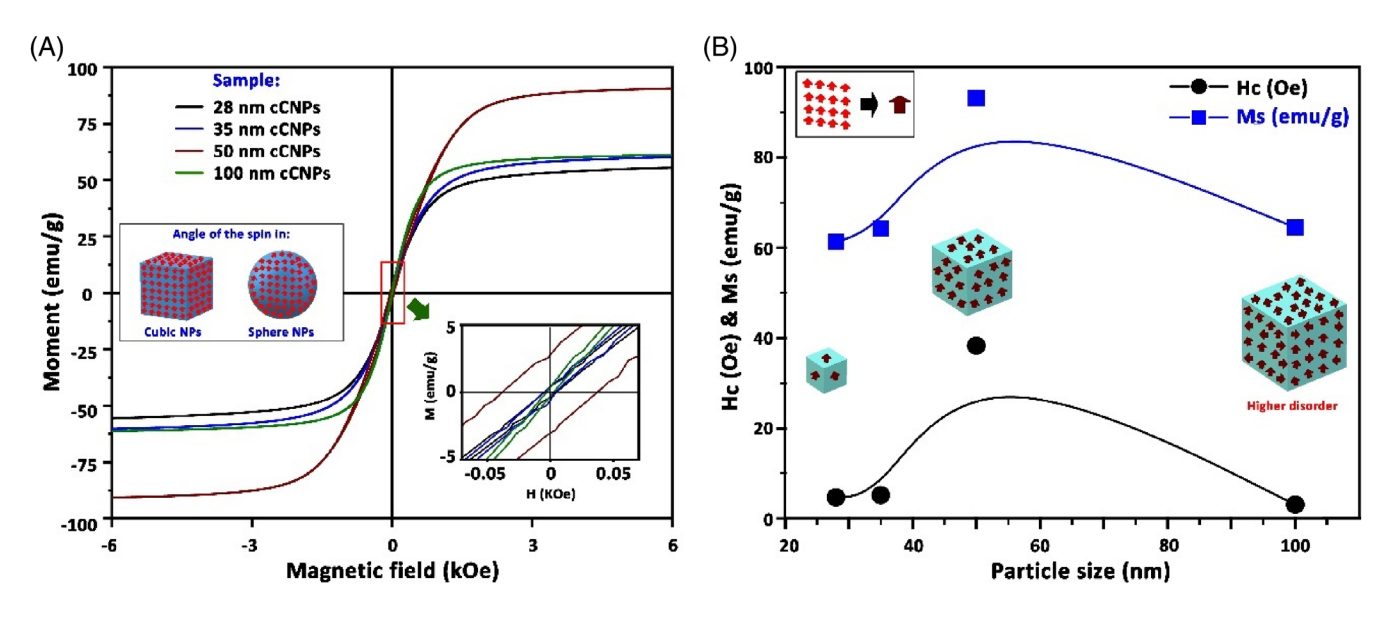


FIGURE 5 Magnetic properties of cCNPs as function of size. (A) Hysteresis loop of different size cCNPs, and (B) M_s and H_c of cCNPs as function of size

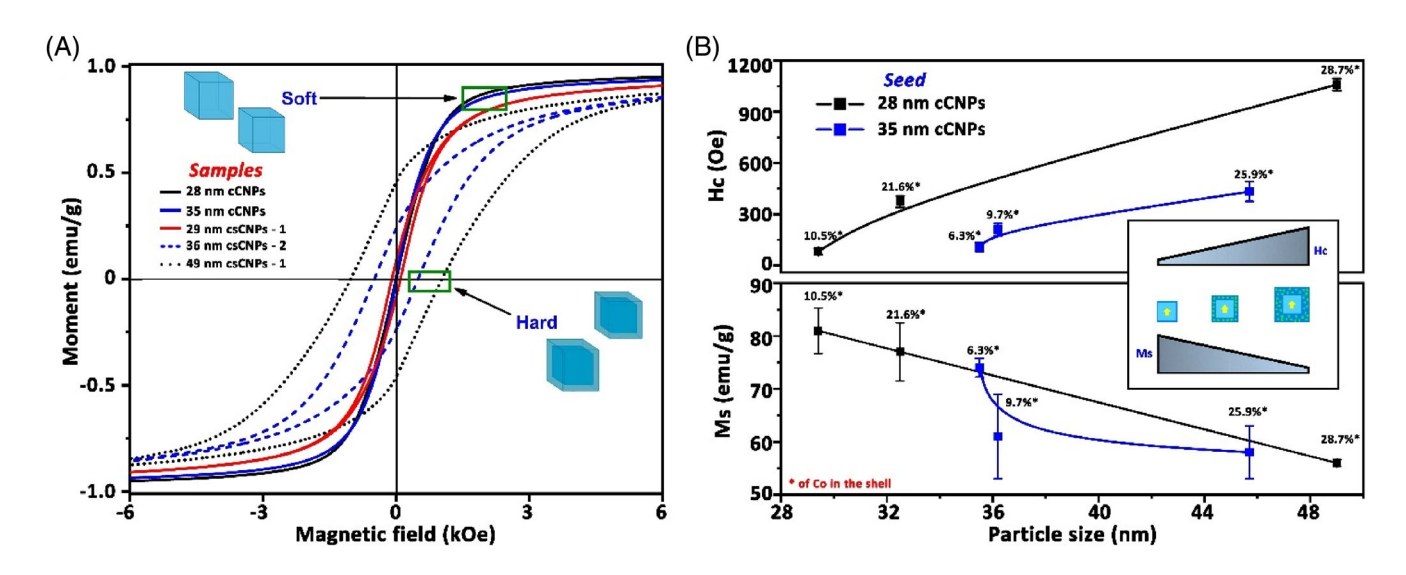


FIGURE 6 Magnetic properties of csCNPs as function of particle size. (A) Hysteresis loops of 28 nm cCNPs, 35 nm cCNPs, 29 nm csCNPs – 1, 36 nm csCNPs – 2 and 49 nm csCNPs – 1. (B) Summary of H_c and M_s for csCNPs

enhanced when the magnetite structure is dopped with a non-ferromagnetic material, although this enhancement produce soft magnetic nanoparticles. 15,16,47 In Figure 6A the hysteresis loops of 28 and 35 nm cCNPs, 29 nm csCNPs – 1, 35 nm csCNPs – 2, and 49 nm csCNPs – 1 are shown. It is possible to observe that hybridization enhances 176 X the H_c in comparison with cCNPs. Figure 6B summarize the H_c and M_s values of all csCNPs synthesized. The coercivity enhancement observed in csCNPs confirms that anisotropy energy was exchanged, supporting the results obtained by XRD. $CoFe_2O_4$ is classified as a hard-magnetic material; however, its H_c is reported around 800 Co. It is known that when a soft- and a hard-magnetic materials are coupled, the soft phase becomes rigidly pinned

by the hard phase at the interface, which allows for an effective exchange coupling. 12,48 Here, it was observed that $H_{\rm c}$ increased as function of the shell thickness (Co concentration increases) up to a saturation point reached in 46 nm csCNPs – 2 and 49 nm csCNPs – 1 (29% and 26% of Co in the shell, respectively), however, $M_{\rm s}$ decreased. 8,12,42,47

To verify the energy conversion efficiency of CNPs, calorimetry measurements were done in aqueous suspensions of particles at a concentration of 1 mg/ml. Calorimetry measurements were done by recording the temperature increment of CNPs suspensions exposed to an AMF of 250 kHz and 27.3 mT for 1 min. SLP was calculated from the slope of the temperature increment and by normalizing for

the heat capacitance of the solvent and the metal content in each sample (Equation (1)). Figure 7 shows the calculated SLP values for cCNPs and csCNPs. It was observed that higher H_c does not necessary translate to higher SLP. The highest SLP value were measured in csCNPs with the thinnest shells (~0.75 nm), being 830 W/g for 36 nm csCNPs – 2 and 1139 W/g for 29 nm csCNPs – 1. The calculated intrinsic loss power (ILP) for these particles are 4.5 nHm²/kg for 36 nm csCNPs – 2, and 6.1 nHm²/kg for 29 nm csCNPs – 1. The discrepancy in the tendency of H_c and SLP could be associated to a lower random spin disorder in the thinnest shells. $^{25,26,28,49-51}$ The increase in the SLP values by the introduction of a CoFe₂O₄ shell

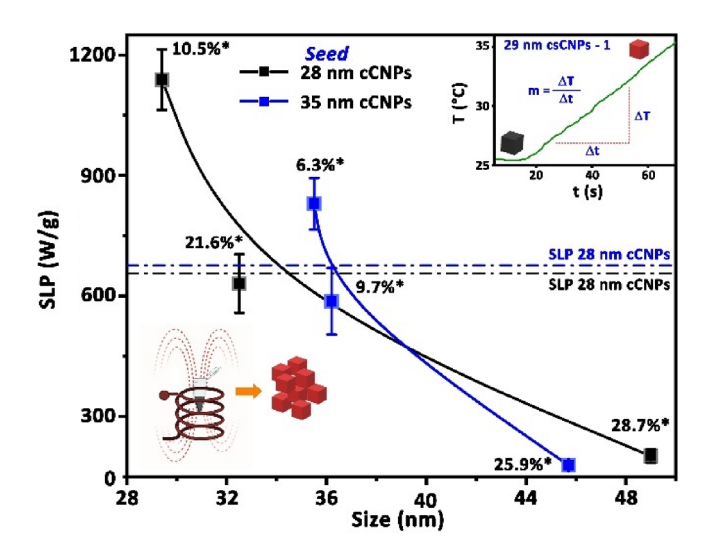


FIGURE 7 SLP of csCNPs as function of Co concentration in the shell

corroborates the successful hybridization and exchange anisotropic effect of the csCNPs. Our results also support the recently proposed hypothesis of systematic nano and atomistic engineering of MNPs' defects and spin disorders to maximize MH³⁴ as the presence of more crystalline defects in the csCNPs with highest SLP was confirmed by XRD diffraction. Table 3 summarizes the calculated SLP and ILP values for the synthesized CNPs and the best values found reported in the literature for ferrite magnetic nanoparticles. The csCNPs synthesized here, displayed some of the highest SLP reported values for synthetic ferrite magnetic nanomaterials. It is important to mention that SLP values are dependent on AMF conditions and that enhanced magnetic heating properties will be found at AMF amplitudes above the coercive field.

3.3 | Magneto-thermal stimulation of neural activity

Calorimetry results show that csCNPs are efficient transducers of AFM into heat. MH has been used for the past few decades in cancer research, ^{34,35,54} and more recently for the remote control of biological signaling. ³¹ 29 nm csCNPs – 1 were tested for the control of heat sensitive ion channels expressed on the cell membrane of primary hippocampal neurons. Hippocampal neurons were co-cultured with 0.1 mg/ml of these csCNPs. Induction of cell activity was studied by applying an AMF of 250 kHz and 27.3 mT to hippocampal neurons co-cultured with csCNPs. The fluorescent calcium indicator Fluo-4 was used to label hippocampal cultures and track neural activity by intracellular calcium influx. When csCNPs are exposed to AMF, they undergo hysteresis power loss dissipating heat. The local heat dissipated by csCNPs should enhance the endogenous temperature

TABLE 3 Summary of magnetic heating properties for different ferrite synthetic nanoparticles

Composition	Size (nm)	Hc (Oe)	f (kHz)	H (kA/m)	SLP (W/g)	ILP (nHm ² /kg)	References
28 nm cCNPs	28	6	250	27.3	567	3.1	This work
35 nm cCNPs	35	5			676	3.6	
29 nm csCNPs - 1	29.4	82			1139	6.1	
33 nm csCNPs - 1	32.5	374			631	3.4	
36 nm csCNPs - 2	35.5	108			830	4.5	
36 nm csCNPs - 2	36.2	210			587	3.1	
46 nm csCNPs - 2	45.7	433			179	1.0	
49 nm csCNPs - 1	49	1139			201	1.1	
CuFe ₂ O ₄	19.9 nm		120	19	44.9	1.0	52
Fe ₃ O ₄	18.5 nm		120	19	18.5	0.4	52
Commercial MIONs						0.15	25
Fe ₃ O ₄	30	33.7	300	15.9	220	2.9	53
$ZnFe_2O_4$	18	62	500	37.4	1860	2.6	
$ZnFe_2O_4$	30	75			2500	3.5	
$ZnFe_2O_4$ / $CoFe_2O_4$	60	1900	500	37.4	10,600	15.1	12

Abbreviations: cCNPs, core cubic magnetic nanoparticles; csCNPs, core-shell cubic magnetic nanoparticles; SLP, specific loss power.

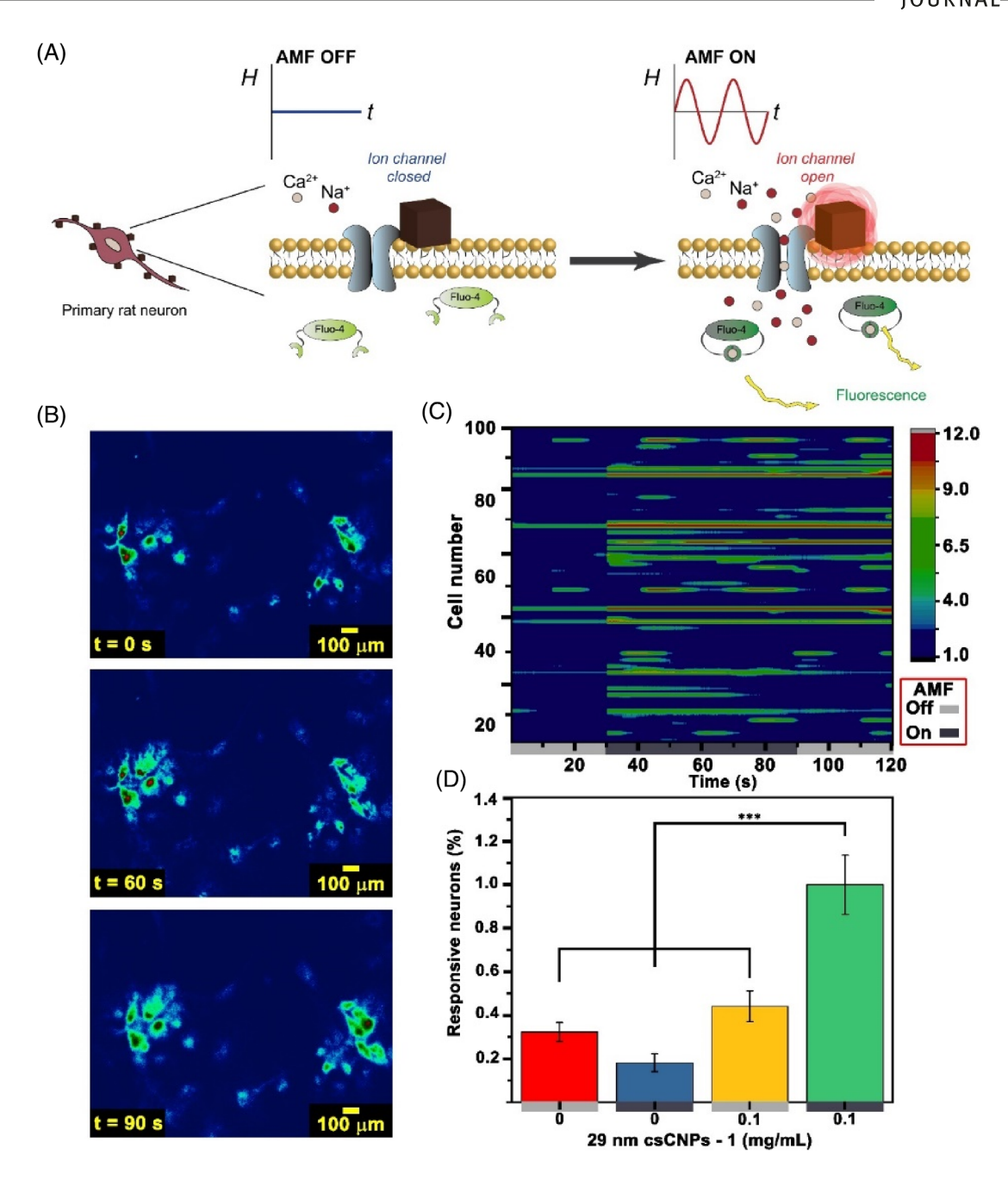


FIGURE 8 Magneto-thermal stimulation of primary hippocampal neurons using 29 nm csCNPs – 1. (A) An overview of the experimental scheme. Hippocampal neurons labeled with Fluo-4 are exposed to csCNPs. Upon exposure to AMF, the heat dissipated by csCNPs triggers the response of endogenous heat-sensitive transmembrane ion channels. These channels respond by gating influx of Calcium ions detectable through Fluo-4. (B) Representative fluorescent calcium images of hippocampal neurons at different times during the stimulation: at t=0 s (prior to AMF), at t=60s (during AMF) and at t=90 s (after AMF). (C) Heat map summarizing the activity of 100 random neurons. (D) Summary of neural responsiveness to magneto-thermal stimulation mediated by csCNPs and AMF (n.s. = no significant difference and ***p < 0.05, one-way ANOVA)

responsive ion channels expressed on the cell membrane of hippocampal neurons, leading to the influx of calcium ions detectable by Fluo-4 dynamic fluorescence (Figure 8A). Induced neural activity in hippocampal neurons co-cultured with 0.1 mg/ml of 29 nm csCNPS – 1 and exposed to AMF is shown in Figure 8. Figure 8B shows representative fluorescent calcium images of hippocampal neurons prior (t=0 s), during (t=60s), and after (t=90s) applying AMF. It is

possible to distinguish an increase in the intracellular calcium concentration during and after applying the AMF. This behavior can be more clearly observed in the Video S1. Figure 8C shows the activity of 100 random neurons prior (t=0 s), during (t=60s), and after (t=90 s) applying the AMF. Figure 8D summarizes the percentage of responsive neurons for the tested groups. The activity of hippocampal neurons co-cultured with 0.1 mg/ml of 29 nm csCNPs – 1 and

exposed to AFM was significantly higher than for those neurons not exposed to AFM stimulation and/or csCNPs. The most remarkable achievement from this preliminary study is that induction of neural activity was detected using $100\times$ less concentration of nanoparticles in comparison with previously reported studies utilizing ferrite spherical nanoparticles. These results corroborate our hypothesis that magnetic anisotropy and surface hybridization can be used for enhancing hysteretic power losses in magnetic nanomaterials. The heat maps summarizing activity of 100 random neurons for the control groups are shown in Figure S6.

Finally, we evaluated the cytotoxic effects of 29 nm csCNPs – 1 with and without AMF stimulation in HEK293 cells by a MTT assay. No cytotoxic effects were found to be associated with csCNPs and or AMF stimulation at the concentrations tested here for magnetothermal neural stimulation (Figure S7).

4 | CONCLUSIONS

The use of magnetic nanoparticles with high efficiency in transducing AMF into heat allows the noninvasive wireless control of biological signaling that could potentially lead to the discovery of novel therapies for the treatment of brain malfunctions. To enhance magnetic heating in ferrite nanomaterials we studied shape and surface anisotropy in CNPs. The magnetic properties of CNPs were optimized by introducing Zn, which modifies the Fe₃O₄ crystal structure increasing their magnetic susceptibility. However, the major enhancement in CNPs magnetic properties was obtained when 28 nm cCNPs (soft) were hybridized with a CoFe₂O₃ shell (hard) at different concentrations of Co in the shell. This hybridization allowed to obtain hard magnetic nanoparticles with 176 X higher H_c compared to core-only same sized CNPs. This enhancement translated into csCNPs with higher heat dissipation efficiency. csCNPs were then utilized as nanotransducers to trigger the response of the heat-sensitive ion channels expressed on the cell membrane of hippocampal neurons. Magneto-thermal neural stimulation utilizing the csCNPs synthesized here resulted in the enhancement of heat sensitive transmembrane channels using 100× less the quantity of particles in comparison with previously reported investigations that utilized spherical ferrite nanoparticles. The ability to decrease magnetic nanoparticles concentration for evoking neural activity will allow to minimize off-target heating effects and increase their potential to be used in biomedical research.

ACKNOWLEDGMENTS

This work was supported in part by the National Science Foundation under a CAREER award to Gabriela Romero (CBET - 2044713). G. Jiménez was supported by The University of Texas System and Mexico's Consejo Nacional de Ciencia y Tecnología through the ConTex Postdoctoral Fellowships Program. The opinions expressed are those of the authors and do not represent views of these funding agencies. The authors would like to thank the technical assistance of Marco A. Leyva from the Chemistry Department of CINVESTAV and Isela Padilla from the Department of Engineering Processes and

Hydraulics at UAM-Iztapalapa. The authors acknowledge the Department of Civil and Environmental Engineering at UTSA for the granted access to the ICP-OES, and the UTSA Kleberg Advanced Microscopy Center for technical support during this work.

AUTHOR CONTRIBUTIONS

The manuscript was written through contributions of all authors. All authors have given approval to the final version of the manuscript. Gloria L. Jiménez carried out experiments, data analysis and wrote the initial draft of this manuscript. Rohini Thevi Guntnur obtained TEM micrographs. Jason Giuliani characterized all the samples by VSM, EDS, and STEM. Gabriela Romero conceived the original idea, supervise the project, wrote, and edited the manuscript.

CONFLICT OF INTERESTS

The authors declare no competing financial interests.

DATA AVAILABILITY STATEMENT

The data that support the findings of this study are available as Supporting Information material through Wiley, or from the corresponding author upon reasonable request.

ORCID

Gabriela Romero https://orcid.org/0000-0001-8081-2946

REFERENCES

- Tudu B, Tiwari A. Recent developments in perpendicular magnetic anisotropy thin films for data storage applications. *Vacuum*. 2017; 146:329-341. https://doi.org/10.1016/j.vacuum.2017.01.031
- Comstock RL. Modern magnetic materials in data storage. J Mater Sci Mater Electron. 2002;13(9):509-523. https://doi.org/10.1023/ A:1019642215245
- Chen R, Christiansen MG, Sourakov A, et al. High-performance ferrite nanoparticles through nonaqueous redox phase tuning. *Nano Lett.* 2016; 16(2):1345-1351. https://doi.org/10.1021/acs.nanolett.5b04761
- Mohapatra J, Mitra A, Tyagi H, Bahadur D, Aslam M. Iron oxide nanorods as high-performance magnetic resonance imaging contrast agents. Nanoscale. 2015;7(20):9174-9184. https://doi.org/10.1039/ c5nr00055f
- Guardia P, Di Corato R, Lartigue L, et al. Water-soluble iron oxide nanocubes with high values of specific absorption rate for cancer cell hyperthermia treatment. ACS Nano. 2012;6(4):3080-3091. https:// doi.org/10.1021/nn2048137
- Okada S, Bartelle BB, Li N, et al. Calcium-dependent molecular fMRI using a magnetic nanosensor. *Nat Nanotechnol*. 2018;13(6):473-477. https://doi.org/10.1038/s41565-018-0092-4
- Ma Y, Li H, Wang L. Magnetic-luminescent bifunctional nanosensors.
 J Mater Chem. 2012;22(36):18761-18767. https://doi.org/10.1039/c2jm32897f
- Lee JH, Kim JW, Levy M, et al. Magnetic nanoparticles for ultrafast mechanical control of inner ear hair cells. ACS Nano. 2014;8(7):6590-6598. https://doi.org/10.1021/nn5020616
- Romero G, Christiansen MG, Barbosa LS, Garcia F. Localized excitation of neural activity via rapid magnetothermal drug release. *Adv Funct Mater*. 2016;26(35):1-8. https://doi.org/10.1002/adfm.201602189
- Qu Y, Li J, Ren J, Leng J, Lin C, Shi D. Enhanced synergism of thermochemotherapy by combining highly efficient magnetic hyperthermia with magnetothermally-facilitated drug release. *Nanoscale*. 2014; 6(21):12408-12413. https://doi.org/10.1039/c4nr03384a

- Sayed FN, Polshettiwar V. Facile and sustainable synthesis of shaped iron oxide nanoparticles: effect of iron precursor salts on the shapes of iron oxides. Sci Rep. 2015;5(March):1-14. https://doi.org/10.1038/ srep09733
- Noh SH, Na W, Jang JT, et al. Nanoscale magnetism control via surface and exchange anisotropy for optimized ferrimagnetic hysteresis. *Nano Lett.* 2012;12(7):3716-3721. https://doi.org/10. 1021/nl301499u
- Hadadian Y, Sampaio DRT, Ramos AP, et al. Synthesis and characterization of zinc substituted magnetite nanoparticles and their application to magneto-motive ultrasound imaging. J Magn Magn Mater. 2018;465(May):33-43. https://doi.org/10.1016/j.jmmm.2018.05.069
- Botta PM, Bercoff PG, Aglietti EF, Bertorello HR, Porto López JM. Synthesis and magnetic properties of zinc ferrite from mechanochemical and thermal treatments of Zn-Fe3O4 mixtures. *Mater Eng.* 2003; A360:146-152.
- Houshiar M, Zebhi F, Razi ZJ, Alidoust A, Askari Z. Synthesis of cobalt ferrite (CoFe2O4) nanoparticles using combustion, coprecipitation, and precipitation methods: a comparison study of size, structural, and magnetic properties. J Magn Magn Mater. 2014;371:43-48. https:// doi.org/10.1016/j.jmmm.2014.06.059
- Lisjak D, Mertelj A. Anisotropic magnetic nanoparticles: a review of their properties, syntheses and potential applications. *Prog Mater Sci.* 2018;95(April):286-328. https://doi.org/10.1016/j.pmatsci.2018. 03 003
- Ali A, Zafar H, Zia M, et al. Synthesis, characterization, applications, and challenges of iron oxide nanoparticles. *Nanotechnol Sci Appl.* 2016;9:49-67.
- Bauer LM, Situ SF, Griswold MA, Samia ACS. High-performance iron oxide nanoparticles for magnetic particle imaging-guided hyperthermia (hMPI). Nanoscale. 2016;8(24):12162-12169. https://doi.org/10. 1039/c6nr01877g
- Hadadian Y, Ramos AP, Pavan TZ. Role of zinc substitution in magnetic hyperthermia properties of magnetite nanoparticles: interplay between intrinsic properties and dipolar interactions. *Sci Rep.* 2019; 9(1):1-14. https://doi.org/10.1038/s41598-019-54250-7
- Roca AG, Gutiérrez L, Gavilán H, Fortes Brollo ME, Veintemillas-Verdaguer S, del Puerto Morales M. Design strategies for shapecontrolled magnetic iron oxide nanoparticles. Adv Drug Deliv Rev. 2019;138:68-104. https://doi.org/10.1016/j.addr.2018.12.008
- Qu X-F, Yao Q-Z, Zhou G-T. Synthesis of siderite microspheres and their transformation to magnetite microspheres. Eur J Mineral. 2011; 23(5):759-770. https://doi.org/10.1127/0935-1221/2011/0023-2134
- Hermosa GC, Chen WC, Wu HS, et al. Investigations of the effective parameters on the synthesis of monodispersed magnetic Fe3O4 by solvothermal method for biomedical applications. AIP Adv. 2020;10 (1):015234-1-015234-7. https://doi.org/10.1063/1.5130063
- Peng E, Wei X, Herng TS, Garbe U, Yu D, Ding J. Ferrite-based soft and hard magnetic structures by extrusion free-forming. RSC Adv. 2017;7(43):27128-27138. https://doi.org/10.1039/c7ra03251j
- 24. David J. Introduction to Magnetism and Magnetic Materials; Chapman and Hall; 1991.
- Liu X, Zhang Y, Wang Y, et al. Comprehensive understanding of magnetic hyperthermia for improving antitumor therapeutic efficacy. *Theranostics*. 2020;10(8):3793-3815. https://doi.org/10.7150/thno. 40805
- Hudson R. Coupling the magnetic and heat dissipative properties of Fe3O4 particles to enable applications in catalysis, drug delivery, tissue destruction and remote biological interfacing. RSC Adv. 2016;6(5): 4262-4270. https://doi.org/10.1039/c5ra22260e
- Reeves DB, Weaver JB. Approaches for modeling magnetic nanoparticle dynamics. Crit Rev Biomed Eng. 2014;42(1):85-93. https://doi.org/10.1615/CritRevBiomedEng.2014010845
- 28. Makridis A, Curto S, Van Rhoon GC, Samaras T, Angelakeris M. A standardisation protocol for accurate evaluation of specific loss

- power in magnetic hyperthermia. J Phys D Appl Phys. 2019;52: 255001.
- Malekigorji M, Curtis ADM, Hoskins C. The use of iron oxide nanoparticles for pancreatic cancer therapy. J Nanomed Res. 2014; 1(1):1-12. https://doi.org/10.15406/jnmr.2014.01.00004
- Bañobre-López M, Teijeiro A, Rivas J. Magnetic nanoparticle-based hyperthermia for cancer treatment. *Rep Pract Oncol Radiother*. 2013; 18(6):397-400. https://doi.org/10.1016/j.rpor.2013.09.011
- Chen R, Romero G, Christiasen M, Mohr A, Anikeeva P. Wireless magnetothermal deep brain stimulation. *Science* (80-). 2015;347: 1477-1480.
- Huang H, Delikanli S, Zeng H, Ferkey DM, Pralle A. Remote control of ion channels and neurons through magnetic-field heating of nanoparticles. *Nat Nanotechnol*. 2010;5(August):602 606. doi:https:// doi.org/10.1038/nnano.2010.125
- Lak A, Disch S, Bender P. Embracing defects and disorder in magnetic nanoparticles. Adv Sci. 2021;8(7):1-14. https://doi.org/10.1002/advs. 202002682
- Moon J, Christiansen MG, Rao S, et al. Magnetothermal multiplexing for selective remote control of cell signaling. Adv Funct Mater. 2020; 30(36):1-9. https://doi.org/10.1002/adfm.202000577
- Chen R, Christiansen MG, Anikeeva P. Maximizing hysteretic losses in magnetic ferrite nanoparticles via model-driven synthesis and materials optimization. ACS Nano. 2013;7(10):8990-9000. https://doi.org/ 10.1021/nn4035266
- Rao S, Chen R, LaRocca AA, et al. Remotely controlled chemomagnetic modulation of targeted neural circuits. *Nat Nanotechnol*. 2019;14(10): 967-973. https://doi.org/10.1038/s41565-019-0521-z
- 37. Zhang T, Ge J, Hu Y, Yin Y. A general approach for transferring hydrophobic nanocrystals into water. *Nano Lett.* 2007;7(10):3203-3207. https://doi.org/10.1021/nl071928t
- Beaudoin GMJ, Lee SH, Singh D, et al. Culturing pyramidal neurons from the early postnatal mouse hippocampus and cortex. *Nat Protoc*. 2012;7(9):1741-1754. https://doi.org/10.1038/nprot.2012.099
- Nasrin S, Chowdhury FUZ, Hoque SM. Study of hydrodynamic size distribution and hyperthermia temperature of chitosan encapsulated zinc-substituted manganese nano ferrites suspension. *Phys B Condens Matter*. 2019;561(February):54-63. https://doi.org/10.1016/j.physb. 2019.02.053
- Haavik C, Stølen S, Fjellvåg H, Hanfland M, Häusermann D. Equation of state of magnetite and its high-pressure modification: thermodynamics of the Fe-O system at high pressure. Am Mineral. 2000;85(3-4):514-523. https://doi.org/10.2138/am-2000-0413
- Nikam DS, Jadhav SV, Khot VM, et al. Cation distribution, structural, morphological and magnetic properties of Co1-xZnxFe2O4 (x = 0-1) nanoparticles. RSC Adv. 2015;5(3):2338-2345. https://doi.org/10. 1039/c4ra08342c
- 42. Varshney D, Verma K, Kumar A. Substitutional effect on structural and magnetic properties of A xCo1-xFe2O4 (A = Zn, Mg and x = 0.0, 0.5) ferrites. *J Mol Struct*. 2011;1006(1–3):447-452. https://doi.org/10.1016/j.molstruc.2011.09.047
- Šepelák V, Tkáčová K, Rykov Al. Rietveld analysis of mechanically activated powdered zinc ferrite. Cryst Res Technol. 1993;28(1):53-56. https://doi.org/10.1002/crat.2170280109
- Volk T, Manfred W. Point defects in LiNbO3. Lithium Niobate (Defects, Photorefracion and Ferroelectric Switching). Springer; 2009:10.
- de Mello LB, Varanda LC, Sigoli FA, Mazali IO. Co-precipitation synthesis of (Zn-Mn)-co-doped magnetite nanoparticles and their application in magnetic hyperthermia. *J Alloys Compd.* 2019;779:698-705. https://doi.org/10.1016/j.jallcom.2018.11.280
- Li Y, Li Q, Wen M, et al. Magnetic properties and local structure studies of Zn doped ferrites. J Electron Spectros Relat Phenomena. 2007; 160(1–3):1-6. https://doi.org/10.1016/j.elspec.2007.04.003

- Chakradhary VK, Ansari A, Akhtar MJ. Design, synthesis, and testing of high coercivity cobalt doped nickel ferrite nanoparticles for magnetic applications. J Magn Magn Mater. 2019;469(February 2018): 674-680. https://doi.org/10.1016/j.jmmm.2018.09.021
- Oezelt H, Kovacs A, Reichel F, et al. Micromagnetic simulation of exchange coupled ferri—/ferromagnetic heterostructures. J Magn Magn Mater. 2015;381:28-33. https://doi.org/10.1016/j.jmmm.2014. 12.045
- Behdadfar B, Kermanpur A, Sadeghi-Aliabadi H, Morales MDP, Mozaffari M. Synthesis of high intrinsic loss power aqueous ferrofluids of iron oxide nanoparticles by citric acid-assisted hydrothermal-reduction route. *J Solid State Chem.* 2012;187:20-26. https://doi.org/10.1016/j.jssc.2011.12.011
- Jadhav SV, Shewale PS, Shin BC, et al. Study of structural and magnetic properties and heat induction of gadolinium-substituted manganese zinc ferrite nanoparticles for in vitro magnetic fluid hyperthermia. *J Colloid Interface Sci.* 2019;541:192-203. https://doi.org/10.1016/j.jcis.2019.01.063
- Liu J, Detrembleur C, Debuigne A, et al. Glucose-, pH- and thermoresponsive nanogels crosslinked by functional superparamagnetic maghemite nanoparticles as innovative drug delivery systems. J Mater Chem B. 2014;2(8):1009-1023. https://doi.org/10.1039/c3tb21272f
- Fotukian SM, Barati A, Soleymani M, Alizadeh AM. Solvothermal synthesis of CuFe2O4 and Fe3O4 nanoparticles with high heating

- efficiency for magnetic hyperthermia application. *J Alloys Compd.* 2020;816:152548. https://doi.org/10.1016/j.jallcom.2019.152548
- Mohapatra J, Xing M, Liu JP. Inductive thermal effect of ferrite magnetic nanoparticles. *Materials (Basel)*. 2019;12(19):26-29. https://doi.org/10.3390/ma12193208
- 54. Ho DN. Magnetic Resonance Imaging and Alternating Magnetic Fields. Elsevier Inc.; 2014.
- 55. Loynachan CN, Romero G, Christiansen MG, et al. Targeted magnetic nanoparticles for remote Magnetothermal disruption of amyloid- β aggregates. *Adv Heal Care Mater.* 2015;14:2100-2109. https://doi.org/10.1002/adhm.201500487

SUPPORTING INFORMATION

Additional supporting information may be found in the online version of the article at the publisher's website.

How to cite this article: Jiménez GL, Thevi Guntnur R, Guiliani J, Romero G. Enhancing magnetic hyperthermia in ferrite nanoparticles through shape anisotropy and surface hybridization. *AIChE J.* 2021;e17437. doi:10.1002/aic.17437